Homogeneous ignition during fuel-rich $H_2/O_2/N_2$ combustion in platinum-coated channels at elevated pressures

CrossMark

Ran Sui, Et-touhami Es-sebbar, John Mantzaras*, Rolf Bombach

Paul Scherrer Institute, Laboratory of Thermal Processes and Combustion, CH-5232 Villigen PSI, Switzerland

ABSTRACT

The hetero-/homogeneous combustion of fuel-rich $H_2/O_2/N_2$ mixtures (equivalence ratios $\varphi = 2.5$-6.5) was investigated experimentally and numerically in a platinum-coated channel at pressures $p = 1$-14 bar. One-dimensional Raman measurements of major gas-phase species concentrations over the catalyst boundary layer assessed the heterogeneous combustion processes, while planar laser induced fluorescence (LIF) of OH at pressures below ~5 bar and of hot-O_2 at pressures above ~5 bar (wherein OH-LIF was not applicable) determined the onset of homogeneous ignition. Simulations were carried out using a 2-D code with detailed hetero-/homogeneous chemical reaction schemes and transport. Both Raman measurements and numerical simulations attested a transport-limited catalytic conversion of the deficient O_2 reactant over the gas-phase induction zones. The agreement between measured and predicted homogeneous ignition distances was better than 12%, thus establishing the aptness of the employed hetero-/homogeneous chemical reaction mechanisms. Analytical homogeneous ignition criteria revealed that the catalytic reaction pathway introduced a scaling factor $1/p$ to the homogeneous ignition distances. This outcome, in conjunction with the intricate pressure dependence of the gaseous ignition chemistry of hydrogen, yielded shorter homogeneous ignition distances at 14 bar compared to 1 bar. The practical implication for gas turbine burners utilizing the catalytic-rich/gaseous-lean combustion concept was that the high operating pressures of such systems promoted the onset of homogeneous ignition within the catalytic module. Sensitivity analysis has finally identified the key catalytic and gaseous reactions affecting homogeneous ignition.

© 2017 The Combustion Institute. Published by Elsevier Inc. All rights reserved.

1. Introduction

In large-scale power generation, hybrid concepts utilizing catalytic (heterogeneous) and gas-phase (homogeneous) combustion have attracted increased attention in the last years [1–3]. One such concept is the catalytic-rich/gaseous-lean combustion, which was originally developed for natural-gas-fueled turbines [3–5]. Therein, part of the air is mixed with all of the natural gas, leading to a reactive mixture with a fuel-rich stoichiometry. This mixture undergoes catalytic partial oxidation (CPO) in a noble-metal-coated catalytic reactor, producing syngas. The syngas products and the unconverted reactants are subsequently mixed with the remaining air, establishing an overall fuel-lean homogeneous combustion zone downstream of the catalytic reactor [6].

The catalytic-rich/gaseous-lean combustion methodology has the advantage of extended extinction limits [4,7], single-digit NO$_x$ emissions and improved flame stability due to the high-hydrogen content of the gaseous combustible mixture [8]. Moreover, this method is applicable not only to natural gas but also to hydrogen and syngas fuels relevant to the current pre-combustion CO_2 capture technologies. For such fuels, the upstream catalytic combustion stage does not entail a CPO function but serves as a preheater and stabilizer for the following homogeneous combustion zone. Integrated combustors based on the catalytic-rich/gaseous-lean approach were developed in the past decade for coal-derived syngas and also for hydrogen [4,9,6]. Finally, while hybrid hetero-/homogeneous combustion is one of the methods pursued in large-scale power generation, it is typically the preferred route in microreactors. This is due to the associated large surface-to-volume ratios and also due to the suppression of undesirable flame instabilities [10–13] by coating the microreactor walls with a catalyst [14,15].

Most of the past fundamental studies on hydrogen hetero-/homogeneous combustion focused on fuel-lean stoichiometries. In terms of numerical simulations, the following works were reported at fuel-lean stoichiometries. Bui et al. [16] simulated the atmospheric pressure combustion of H_2/air mixtures over Pt-coated stagnation point flow surfaces, Meyet et al. [17] simulated the

* Corresponding author.
E-mail address: ioannis.mantzaras@psi.ch (J. Mantzaras).

Nomenclature

c_p	gas heat capacity
Da_g	gas-phase Damköhler number, Eq. (4)
b	half-height of catalytic reactor, Fig. 1
L	length of catalytic reactor, Fig. 1 and Eqs. (2), (3), (5)
Le_k	Lewis number of k-th gaseous species (thermal over mass diffusivity)
p	pressure
Re_{IN}	inlet Reynolds number, Eq. (3)
T_{IN}	inlet temperature of gas
U_{IN}	inlet streamwise velocity, Eq. (3)
v', v''	vibrational quantum numbers of upper and lower state, Fig. 4
W	width of catalytic reactor, Fig. 1
x, y, z	streamwise, transverse, and spanwise coordinates, Fig. 1
x_{ig}	homogeneous ignition distance, Figs. (6) and (9)

Greek Symbols

$\alpha_{th,IN}$	thermal diffusivity of gas at inlet, Eq. (6)
ζ_{ig}	normalized homogeneous ignition distance, Eq. (2)
λ	gas thermal conductivity, Eq. (6)
μ	gas dynamic viscosity, Eq. (3)
ρ	gas density, Eqs. (3) and (6)
τ_{ch}	characteristic gas-phase chemical time, Eqs. (4), (7) and (8)
τ_{dif}	characteristic transverse diffusion time, Eqs. (4) and (5)
τ_{ig}	ignition delay, Fig. 13
φ	hydrogen-to-oxygen equivalence ratio

Subscripts

IN	inlet

combustion of $H_2/O_2/N_2/H_2O$ mixtures in a Pt-coated channel at atmospheric pressure, while Andrae and Björnbom [18] studied the impact of boundary conditions (Pt-coated versus chemically inert walls) on the homogeneous ignition of H_2/air mixtures. In terms of experiments, Appel et al. [19] applied laser-based measurements of major and minor species concentrations across the boundary layer of a platinum-coated channel at atmospheric pressure and, in conjunction with numerical simulations, assessed the validity of various hetero-/homogeneous chemical reaction schemes for fuel-lean H_2/air mixtures and the conditions leading to the onset of homogeneous ignition. Mantzaras et al. [20] and Ghermay et al. [21] extended the work of Appel et al. [19] to pressures up to 15 bar, while Ghermay et al. [22] investigated the impact of water vapor addition on the combustion of fuel-lean $H_2/O_2/N_2/CO_2$ mixtures over platinum at moderate pressures up to 8 bar.

For fuel-rich stoichiometries there have been fewer fundamental hetero-/homogeneous combustion studies of hydrogen. Bui et al. [16] investigated numerically not only fuel-lean but also fuel-rich H_2/air stoichiometries. Maestri et al. [23,24] studied experimentally and numerically the atmospheric pressure hetero-/homogeneous combustion of fuel-rich H_2/air mixtures in a Rh-coated annular channel with a gap of 2.1 mm. Schultze et al. [25] applied in situ Raman measurements and planar Laser Induced Fluorescence (LIF) of the OH radical to evaluate the catalytic and gas-phase combustion processes of fuel-rich $H_2/O_2/N_2$ mixtures in a Pt-coated, 7-mm-height rectangular channel at pressures up to 5 bar; the sharp drop of the OH-LIF signal with rising pressure at rich stoichiometries precluded measurements at $p > 5$ bar. More recently, we introduced the methodology of OH-LIF at pressures below ~5 bar and of hot O_2-LIF at $p > 5$ bar to

study homogeneous ignition of fuel-rich syngas mixtures over Pt at pressures up to 14 bar [26]. However, investigations of hydrogen hetero-/homogeneous combustion at fuel-rich stoichiometries and turbine-relevant pressures (up to 15 bar) applicable to the catalytic-rich/gaseous-lean combustion methodology are still lacking. Hydrogen gas-phase chemistry exhibits intricate pressure dependence [27] and its coupling with the catalytic pathway, which can have its own pressure dependence, has not been elaborated in the past especially regarding the implications for the onset of homogeneous ignition. Moreover, at fuel-rich stoichiometries the Lewis number of the deficient reactant (oxygen) is larger than unity and this can introduce large differences to the flame shapes and flame locations (and hence to the gaseous consumption of the limiting reactant in the catalytic channel) compared to fuel-lean stoichiometries [19] where the Lewis number of the deficient reactant (hydrogen) is less than unity.

The present paper undertakes an experimental and numerical investigation of the hetero-/homogeneous combustion characteristics of fuel-rich (equivalence ratios $2.5 \leq \varphi \leq 6.5$) $H_2/O_2/N_2$ mixtures at pressures of 1–14 bar. Experiments are performed in an optically accessible, Pt-coated catalytic channel reactor with a height of 7 mm and a length of 300 mm. 1-D Raman measurements yield the major gas-phase species concentrations over the catalyst boundary layer. Homogeneous combustion is monitored with planar LIF of the OH radical up to 5 bar and with planar LIF of hot-O_2 at higher pressures. Simulations are carried out with an elliptic 2-D code, which includes detailed catalytic and elementary gaseous chemical reaction schemes and detailed transport.

A main objective is to provide validated hetero-/homogeneous chemical reaction schemes at turbine-relevant pressures up to 14 bar. Heterogeneous reaction mechanisms, in particular, have not been validated at such pressures. Furthermore, gas-phase reaction mechanisms have not been tested at the very large fuel-rich stoichiometries (hydrogen-to-air equivalence ratios ~20), which are attained at the locations of homogeneous ignition due to the upstream catalytic depletion of the limiting oxygen reactant. The validation is finally crucial given the chemical interactions between the catalytic and gaseous reaction pathways. Additional objectives are, by using the validated hetero-/homogeneous reaction mechanisms, to assess the impact of pressure on the homogeneous ignition characteristics, to compare the flames formed under rich stoichiometries to those reported earlier at lean stoichiometries, and finally to study the hetero-/homogeneous chemistry interactions at elevated pressures.

This paper is organized as follows. The experimental and numerical methodologies are presented in Sections 2 and 3, respectively. The assessment of homogeneous ignition with the two employed methodologies (OH-LIF and hot-O_2-LIF) is elaborated in Section 4.1, while comparisons between measurements and predictions in Sections 4.2 and 4.3 are used to assess the aptness of the employed chemical reaction schemes. The impact of pressure on homogeneous ignition along with a sensitivity analysis identifying the key catalytic and gaseous reactions affecting homogeneous ignition are discussed in Section 4.4, and finally the main conclusions are summarized in Section 5.

2. Experimental

The experimental setup (Fig. 1) has been described elsewhere [21], such that only details relevant to the present study are given. The test-rig consisted of: a) a high pressure, optically accessible channel-flow catalytic reactor, b) an optical setup for planar LIF of OH and of hot-O_2, and c) an optical setup for 1-D Raman measurements of major gas-phase species concentrations across the channel height.
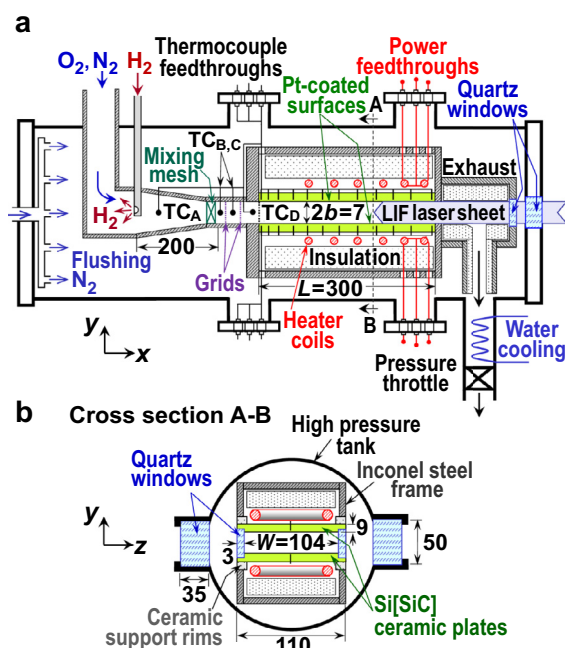
Fig. 1. High pressure catalytic combustion test rig. All distances are in mm.

Table 1
Experimental conditions[a].

Case	p	φ	U_{IN}	T_{IN}	H_2	O_2	N_2
1[b]	1	2.5	3.90	317	29.4	5.8	64.8
2[b]	1	6.5	4.67	306	73.2	5.7	21.1
3[b]	3	3.5	1.20	301	40.9	5.9	53.2
4[b,c]	3	6.5	1.48	296	73.2	5.7	21.1
5[b]	5	6.5	0.90	297	73.2	5.7	21.1
6[c]	6	2.5	0.63	302	35.7	7.1	57.2
7[b,c]	6	6.0	0.80	296	77.5	6.4	16.1
8[c]	9	2.5	0.43	303	38.4	7.7	53.9
9[c]	12	3.5	0.42	298	70.2	10.0	19.8
10[c]	14	2.5	0.32	298	55.4	11.1	33.5
11[d]	4	6.5	1.10	294	73.2	5.7	21.1
12[d]	9	3.5	0.43	297	50.0	7.1	42.9

[a] Pressure p (bar), equivalence ratio φ, inlet velocity U_{IN} (m/s), inlet temperature T_{IN} (K), and volumetric compositions (%) of H_2, O_2 and N_2
[b] Cases with –OH-LIF measurements
[c] Cases with O_2-LIF measurements
[d] Cases with Raman measurements

2.1. High pressure test rig

Experiments were performed in an optically accessible catalytic channel-flow reactor. The channel enclosure was formed by two horizontal ceramic plates made of Si[SiC] and two vertical quartz windows with a thickness of 3 mm (see Fig. 1(b)). The Si[SiC] plates had a length L = 300 mm (-x), a width W = 104 mm (-z), and a thickness of 9 mm, and were placed at a distance $2b$ = 7 mm (-y) apart. The inner Si[SiC] surfaces were firstly coated by a 1.5 µm thick non-porous alumina layer (Al_2O_3) and then by a 2.2 µm thick Pt layer using plasma vapor deposition (PVD). The Al_2O_3 layer mitigated chemical interactions between Pt and Si. The 2.2 µm thick platinum layer resembled a polycrystalline Pt surface, and this was verified with total and active surface measurements using BET (Kr-physisorption) and CO-chemisorption, respectively [28].

The reactor assembly was mounted inside a high-pressure cylindrical steel tank, which was equipped with two $350 \times 50 \times 35$ mm^3 quartz side windows (Fig. 1(b)). Two additional quartz windows at the rear tank flange and the reactor exhaust

(Fig. 1(a)) provided an axial optical access for the LIF laser beams. The outer Si[SiC] surfaces were heated by two adjustable-power resistive coils over the length 100 mm < x < 300 mm in order to control the catalyst surface temperatures. S-type thermocouples (12 for each Si[SiC] plate), positioned along the x–y symmetry plane (Fig. 1(a)) and embedded 0.9 mm beneath the catalyst, monitored the surface temperatures.

High-purity H_2 (99.995%), N_2 (99.998%) and O_2 (99.7%) gases were supplied by batteries and their flows were regulated by three dedicated Brooks mass flow controllers. Hydrogen was injected counterflow to the O_2/N_2 mixture inside a 200-mm-long steel conical section (which was specifically designed to mitigate autoignition of the pressurized reactive mixture) by means of eight 0.5-mm-diameter nozzles arranged horizontally along the z-direction (see Fig. 1(a)). The conical section gradually adjusted its cross sectional area from circular (35 mm diameter) to the final rectangular channel shape (104×7 mm^2). The gases were mixed in a 3-mm-thick mesh and two grids (0.4×0.4 mm^2 open size) that ensured mixture homogeneity and flow uniformity. Optimization of the number and axial positions of the mesh/grids was accomplished by the following room temperature measurements performed at the exit plane of the stand-alone conical unit: a) hot wire velocimetry to assess flow uniformity, and b) planar LIF of NO (doped into the hydrogen stream, excitation at 226.25 nm and detection at 240-265 nm) to assess the mixing quality of H_2 with O_2/N_2.

Experiments were carried out at fuel-rich stoichiometries, with hydrogen-to-oxygen equivalence ratios φ = 2.5–6.5. To control homogeneous ignition at different pressures, a variable nitrogen dilution was used, with the N_2 volumetric content ranging from 16.1% to 64.8% (see Table 1). The gas temperature at the reactor inlet, T_{IN}, was measured by a K-type thermocouple (marked as TC_D in Fig. 1(a)), whose bead was radiation-shielded by enclosing it inside a 1.2-mm-ID and 2.0-mm-OD ceramic tube. The inlet velocities were U_{IN} = 0.32-4.67 m/s, yielding laminar flows with incoming Reynolds numbers 730-1149 based on the full channel height $2b$ = 7 mm and the inlet gas properties. It is noted that laminar flow conditions were guaranteed even at considerably higher inlet Reynolds numbers (~5000) due to the strong flow laminarization induced by the heat transfer from the hot catalytic walls [29]. The pressure was varied in the range 1-14 bar, while the inlet temperatures were T_{IN} = 294-317 K, due to a modest preheat of the conical mixing section via conduction from the hot reactor. Three thermocouples (TC_A, TC_B and TC_C in Fig. 1(a)) upstream of the channel reactor monitored the gas temperature inside the mixing section.

2.2. Laser diagnostics

2.2.1. OH-LIF

The optical setup for the planar OH-LIF is depicted in Fig. 2. A pulsed Nd:YAG laser (YG981E/IR-20 LC D4 LNE, 10 ns pulse duration and 20 Hz repetition rate) was combined with a dye laser (Quantel TDL90 NBP2UVT3). The 532 nm second harmonic of the Nd:YAG laser pumped a 10% (RhB/Rh6G) mixture dye and the radiation output was frequency doubled to produce the excitation beam at 282.93 nm with an energy of 2 mJ/pulse. The 282.93 nm radiation excited the well-characterized $Q_1(6)$ band of the OH electronic transition $A^2\Sigma$ (ν = 1) $\leftarrow$ $X^2\Pi$ (ν' = 0). A cylindrical lens and a slit mask created a collimated light sheet approximately 300 µm thick, which propagated counterflow along the reactor's x–y symmetry plane (see Fig. 2).

Fluorescence was collected at 90° with respect to the incoming laser beam with an ICCD camera (LaVision Imager Compact HiRes IRO, 1392×1024 pixels). The camera was equipped with appropriate filters to collect fluorescence from the OH (1–1) and (0–0) bands at wavelengths between 308 and 314 nm. Channel areas of 100×7 mm^2 (in x-y) were recorded on 628×44 pixels of the CCD
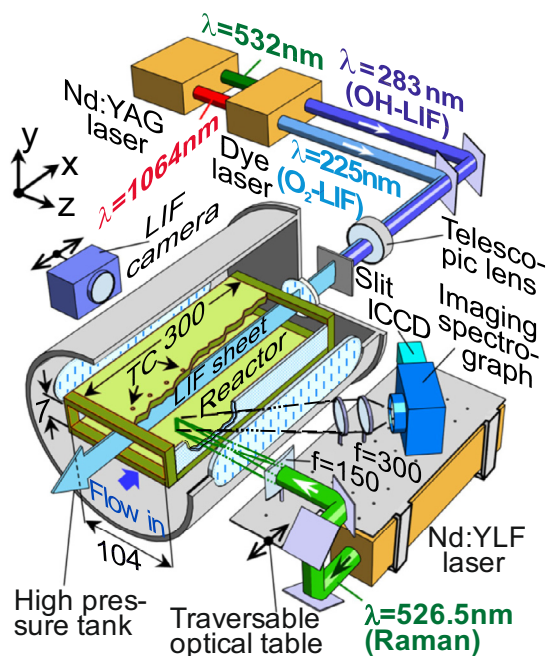
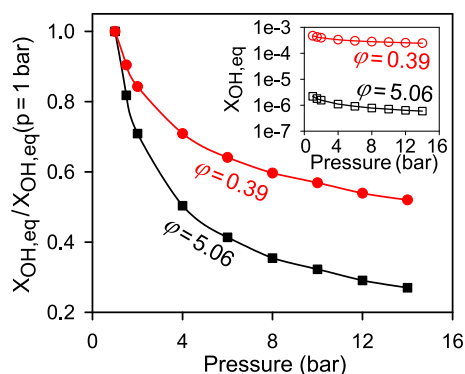**Fig. 2.** Optical setups for the planar OH-LIF, planar O_2-LIF and 1-D Raman. All distances and focal lengths are in mm.

Fig. 3. Computed equilibrium OH mole fraction as a function of pressure at two H_2/air equivalence ratios (lean $\varphi = 0.39$ and rich $\varphi = 5.06$) with the same adiabatic equilibrium temperature and initial temperature of 673 K.

Fig. 4. Simplified energy level diagram with the selected electronic transition for excitation (λ_e), and the observed fluorescence wavelengths (λ_f) for hot O_2-LIF measurements.

ing the pressure from 3 to 6 bar, the OH-LIF signal dropped rapidly and fell below the detection limits at higher pressures.

2.2.2. O_2-LIF

O_2-LIF for flame imaging has been reported in [31–33], while its application to hetero-/homogeneous systems was demonstrated in our earlier study of fuel-rich syngas/air combustion over Pt at elevated pressures [26]. Radiation at 225.06 nm was used to excite the R(19) line of the B ← X ($v'= 2$, v''=4) transition of the O_2 molecule. Fluorescence was collected at 90° from the B → X ($2 - n$, $n = 8$, 9, 10) transitions at wavelengths between 260 and 290 nm. Simplified electronic transition excitation and fluorescence detection schemes are shown in Fig. 4. Excitation at 225.06 nm offered an advantage, as it could be produced by mixing the radiation at ~283 nm (which was already available from the OH-LIF excitation) with the fundamental 1064 nm radiation of the Nd:YAG laser.

The 225.06 nm radiation (energy ~0.5 mJ/pulse) was transformed into a vertical light sheet propagating counterflow on the same plane as the OH-LIF beam (see Fig. 2). Similar to the OH-LIF, the imaged area on the CCD camera was 100×7 mm^2. Four dielectric reflection filters (Laser Optik GmbH) and additional colored glass filters were used to eliminate unwanted background signals and to improve the signal-to-noise ratio. Typically 1200 O_2-LIF images were averaged at each measuring position.

To ensure that only O_2 molecules were excited without interference from other species, Fig. 5(a) provides the measured (in an atmospheric pressure, propane-fueled Bunsen burner at a temperature of 1800 K) excitation spectrum of the *Schumann-Runge* O_2 band transition in the range 225.01-225.19 nm, which naturally contained contributions from other species (notably NO). Simulated excitation spectra of O_2 and of the NO ($A^2\Sigma \leftarrow X^2\Pi$) band (which can overlap with O_2), obtained using the LIFsim package [34] at the same pressure and temperature are also shown in Fig. 5(a). The selected R(19) line minimized interferences from adjacent NO lines, as predicted from the LIFsim [34]. Additional LIFsim predictions have verified that the R(19) line was unaffected by NO interferences at pressures up to 14 bar.

The plot of the O_2-LIF signal as a function of the laser energy in Fig. 5(b) has a slope of 0.9 ± 0.1 over a wide range of laser intensities (~0.1–10 mJ), implying that no saturation effects had to be considered. Contrary to the case of OH-LIF, at low pressures the predissociation of the excited state of O_2 was so fast that quenching effects remained negligible. However, at elevated pressures

detector chip, leading to a 160 μm/pixel spatial resolution. The camera was traversed axially to record the entire channel length. To increase the signal-to-noise ratio in the present stationary operating conditions, 1200 OH-LIF images were averaged at each measuring axial location.

While the OH radical is a commonly-used marker for gaseous combustion, OH-LIF does not suffice at elevated pressures and rich H_2/O_2 stoichiometries [25]. Figure 3 provides the computed equilibrium mole fraction of OH (X_{OH}, calculated with the equilibrium code of Chemkin [30] at constant pressure and total enthalpy) as a function of pressure for a lean ($\varphi = 0.39$) and a rich ($\varphi = 5.06$) stoichiometry; X_{OH} is normalized by the corresponding values at 1 bar (for absolute values, see inset in Fig. 3). The initial gas temperature in the equilibrium simulations was 673 K, while the specific lean and rich equivalence ratios were selected to yield nearly the same adiabatic equilibrium temperature (≈ 1726 K). For the rich stoichiometry the OH mole fraction dropped faster with rising pressure and, moreover, the absolute X_{OH} was substantially lower. The low OH concentrations negated the use of OH-LIF at rich stoichiometries and elevated pressures. Already when increas-
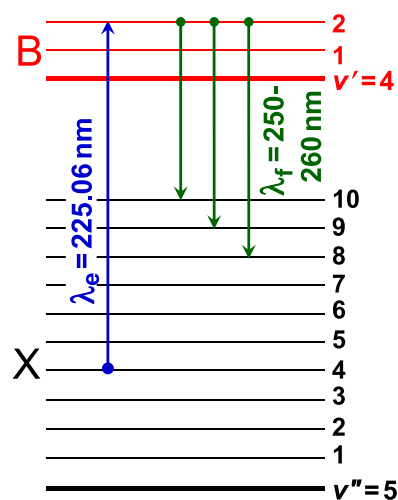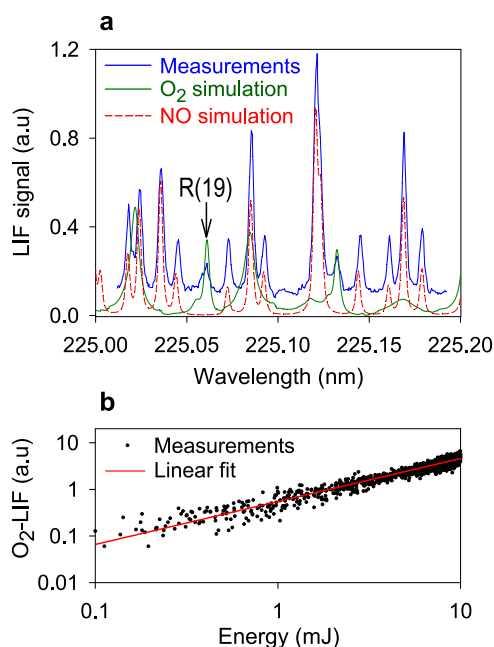
Fig. 5. (a) Measured and simulated O$_2$-LIF spectra at $p = 1$ bar and $T = 1800$ K. The simulated NO excitation spectrum, which can overlap with O$_2$, is also shown under the same conditions. The selected R(19) line is marked by an arrow. Simulations are performed using LIFsim [34]. (b) log–log plot of fluorescence signals of O$_2$ molecules versus the UV laser energy.

(above approximately 12 bar) collisional processes became important, such that the collisional quenching of the excited state as well as the O$_2$ predissociation rate had to be considered for a quantitative analysis. Since goal of the present study was to only identify the flame location, quantification of O$_2$-LIF was not necessary.

For pressures above ~5 bar the OH-LIF signal-to-noise was too low for detection due to low concentration and line broadening. On the other hand, the predissociative nature of O$_2$ molecules was beneficial for high pressure O$_2$-LIF (i.e. $p > 5$ bar), as it masked all effects of collisional quenching below ~12 bar. The linear increase of concentration with pressure at constant mole fraction led to an increase of the signal. Consequently, the O$_2$-LIF signal abruptly overtook the OH-LIF signal above about 5 bar.

2.2.3. Raman measurements

To assess the catalytic processes preceding the onset of homogeneous ignition, measurements of major gaseous species concentrations were performed using the Raman technique. For this purpose, a frequency-doubled pulsed Nd:YLF laser (Quantronix Darwin-Duo 80), with a pulse energy of 43 mJ at 526.5 nm was employed (see Fig. 2). The pulse duration and repetition rate were 130 ns and 2 kHz, respectively. A cylindrical lens with a focal length of 150 mm focused the 526.5 nm laser beam into a vertical line with a thickness of 300 μm. The focal line spanned the entire 7 mm channel height and was offset laterally (z-direction) from the x-y symmetry plane by 15 mm, leading to a sufficiently large collection solid angle for the scattered light.

The Raman-scattered light was collected at a 50° angle via two broadband antireflection coated lenses (75-mm diameter, focal lengths of 300 mm) and was focused to the 25 μm slit of a 25 cm spectrometer (Chromex-250i), which was equipped with an intensified CCD camera (Princeton Instruments PI-MAX1024GIII). The Nd:YLF laser, the sending/collecting optics and the spectrometer were all mounted on a traversable optical table, allowing measurements over the initial 150 mm axial extent of the reactor. To increase the signal-to-noise ratio, Raman-scattered light from up

to 300,000 laser pulses was integrated on the detector chip. The 1024×256 pixel CCD dimensions corresponded to spectral shift and transverse position, respectively. The 7 mm channel height corresponded to 210 pixels, which were subsequently binned to 63. Raman cross-sections were evaluated by recording signals of known composition H$_2$/O$_2$/N$_2$ mixtures under non-reactive isothermal conditions at the beginning of the catalytic channel. Details about the Raman measurements can be found in our previous studies [21,26].

3. Numerical

Numerical simulations were carried out using the 2-D steady CFD code of PSI, described in previous works [35, 28, 21]. The 300×7 mm^2 reactor domain was discretized by 2600×68 grid points (in -x and -y, respectively, with uniform spacing in –x and finer spacing towards the walls in –y). The x-direction had a coarser resolution (115 μm), but it was sufficient to resolve the ensuing flames: the thermal flame thicknesses, calculated using the 1-D Premix code of Chemkin [36] (see further discussion in Section 4.1) and defined as the lengths encompassing 5–95% of the temperature rise, ranged from 565 to 980 μm. Uniform inlet species mass fractions, temperature and axial velocity were imposed at the entry and zero Neumann boundary conditions were applied at the exit. The energy boundary conditions at the upper and lower channel walls were prescribed axial temperature profiles, constructed by fitting a curve through the twelve thermocouple measurements on each plate. The governing equations have been presented elsewhere [21] and are not repeated here.

The detailed mean-field reaction mechanism for the oxidation of hydrogen on platinum by Deutschmann et al. [37] was used (14 reactions, 9 surface and 5 gas-phase species, surface site density of 2.7×10^{-9} mol/cm^2) along with the elementary gaseous reaction mechanism by Li et al. [38] (21 reversible reactions and 9 species). Catalytic and gaseous reaction rates were evaluated with Surface-Chemkin [39] and Chemkin [40], respectively. Mixture-average diffusion including thermal diffusion for the light species was used, with transport parameters assessed from the Chemkin transport database [41].

4. Results and discussion

The assessment of homogeneous ignition with the two LIF techniques is discussed first, comparisons of measurements and predictions follow, the heterogeneous and homogeneous combustion processes are subsequently elaborated, and finally the impact of pressure on homogeneous ignition is addressed.

4.1. Assessment of homogeneous ignition with OH-LIF and hot O$_2$-LIF

Comparisons between measured OH-LIF and O$_2$-LIF signals and predicted OH and hot O$_2$ mole fraction distributions are shown in Fig. 6 for Cases 4 and 7 referring to moderate pressures of 3 and 6 bar, respectively, where both types of LIF measurements were possible. The measurements in Fig. 6 were constructed using 100–mm–long, partially overlapping images, either for OH-LIF or hot-O$_2$-LIF.

To facilitate comparisons between the LIF-measured and numerically predicted hot O$_2$, the Boltzmann distribution was used to derive the fraction of hot O$_2$ molecules in the excited level (v' = 4). This was in turn proportional to the temperature and the energy separation ($\Delta\varepsilon$) from the lower vibrational energy level ($v'=0$), which was $\Delta\varepsilon = 0.744$ eV [42]. Assuming a molecular partition function over all energy states equal to 1, the fraction of O$_2$ molecules in the excited sate was given by $n_{O2}/N = \exp(-\Delta\varepsilon/K_BT)$, with K_B the Boltzmann constant and T the gas temperature.
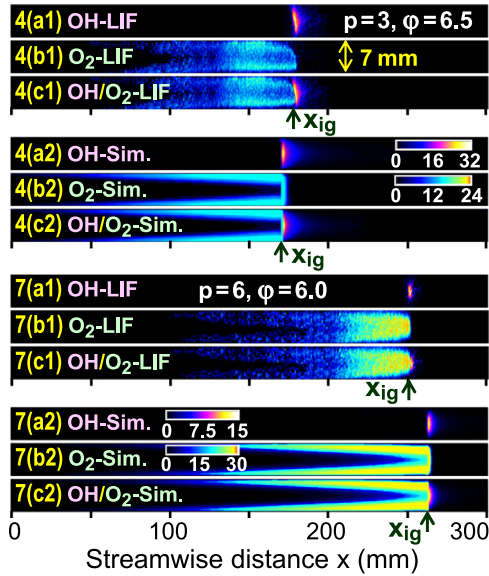
Fig. 6. Planar LIF measurements of: (a1) OH, (b1) hot-O_2, (c1) superposition of OH/hot-O_2 LIF. Simulations: (a2) OH (color bar in ppmv), (b2) hot-O_2 (color bar in ppmv) and (c2) superposed OH/hot-O_2. Results are shown for Case 4 ($p = 3$ bar, $\varphi = 6.5$) and Case 7 ($p = 6$ bar, $\varphi = 6.0$) in Table 1. The vertical arrows marked x_{ig} indicate the homogeneous ignition locations. (For interpretation of the references to color in this figure legend, the reader is referred to the web version of this article).

Fig. 7. (a) Measured axial profiles of OH-LIF and hot-O_2-LIF signals, and (b) predicted axial profiles of OH and hot-O_2 along the mid-plane ($y = 3.5$ mm) for Case 4 in Fig. 6. The symbols indicate the 50% rise of OH (circles) and of hot-O_2 (triangles). For clarity, OH is divided by 6.

The homogeneous ignition locations in Fig. 6 were denoted by vertical arrows marked x_{ig}. In the OH-LIF images, x_{ig} were defined as the far-upstream locations along the channel mid-plane ($y = 3.5$ mm) where the OH-LIF signal rose to 50% of the maximum mid-plane value. Likewise, homogeneous ignition in the O_2-LIF images was defined as the far-upstream location along the mid-plane, where the O_2-LIF signal rose to 50% of its maximum mid-plane value. The same homogeneous ignition definitions were also applied to the simulations of Fig. 6, using the predicted OH and hot-O_2 mole fractions. The above definitions yielded similar homogeneous ignition distances for the two employed LIF techniques as shown in Fig. 7, referring to Case 4 in Fig. 6. Characteristically, the measured 50% rise of OH and hot-O_2 LIF signals along the mid-plane differed in Fig. 7(a) by less than a pixel (160 μm/pixel resolution), while the simulations in Fig. 7(b) had a corresponding difference less than the axial numerical resolution of 115 μm.

The definition of homogeneous ignition using either OH or O_2 has been further elaborated by computing with a high resolution the laminar flame structure of rich hydrogen flames in Fig. 8, using the 1-D Premix package of Chemkin [36]. The plots in Fig. 8 emphasized the flame parts around the peaks of OH and hot-O_2, while the simulation conditions mimicked Cases 4 and 7, respectively. To this purpose, the initial temperatures and equivalence ratios for the 1-D flame simulations were taken from the 2-D simulations of Cases 4 and 7 just upstream of the ignition locations x_{ig} (these quantities were averaged over the 7-mm channel height). Note that the depletion of the limiting O_2 reactant by the catalytic pathway over the gaseous induction zone $0 \leq x < x_{ig}$ resulted in richer equivalence ratios just upstream of x_{ig} compared to those at the channel entry given in Table 1 (from all cases in Table 1, the highest equivalence ratio just upstream of homogeneous ignition was 19.8). Similarly, the heat transfer from the hot catalytic walls over the gaseous induction zone augmented the mixture preheat. The hot O_2, derived from the Boltzmann distribution according to the procedure discussed at the beginning of this section, is also plotted in Fig. 8.
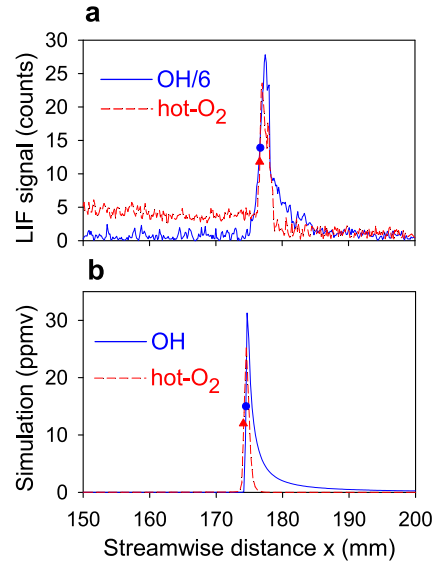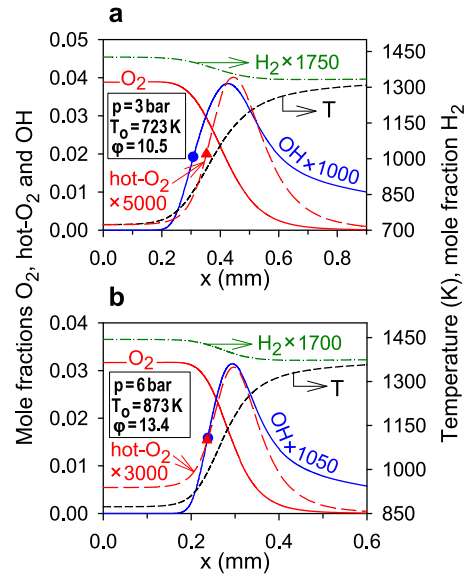

Fig. 8. Computed 1-D laminar flame structure at fuel-rich compositions and preheats, mimicking Cases 4 and 7 in Table 1: the O_2, OH, H_2, hot-O_2 mole fractions and the temperature are plotted. (a) $p = 3$ bar, $T = 723$ K, $\varphi = 10.5$ (b) $p = 6$ bar, $T = 873$ K, $\varphi = 13.4$. Triangles and circles denote the far-upstream positions where OH and hot-O_2 rose to 50% of their peak flame values, respectively.

The upstream location of 50% OH rise (circles in Fig. 8) and of 50% hot-O_2 rise (triangles in Fig. 8) differed by 45 μm in Fig. 8(a) and by 2 μm in Fig. 8(b), i.e. lengths corresponding to 1.3–28.1% of the experimental pixel resolution. The agreement between measured and predicted homogeneous ignition positions in Fig. 6 was very good (either using the OH or the hot-O_2 methodology), and the same applied for the 2-D OH distributions. On the other side, the measured hot-O_2 mole fraction distributions upstream of homogeneous ignition were somewhat broader in the transverse (-y) direction than the corresponding simulations (e.g. compare Figs. 6(4b1) and 6(4b2) or Figs. 6(7b1) and 6(7b2)). Nonetheless, this was not a crucial issue as the present work focused on the
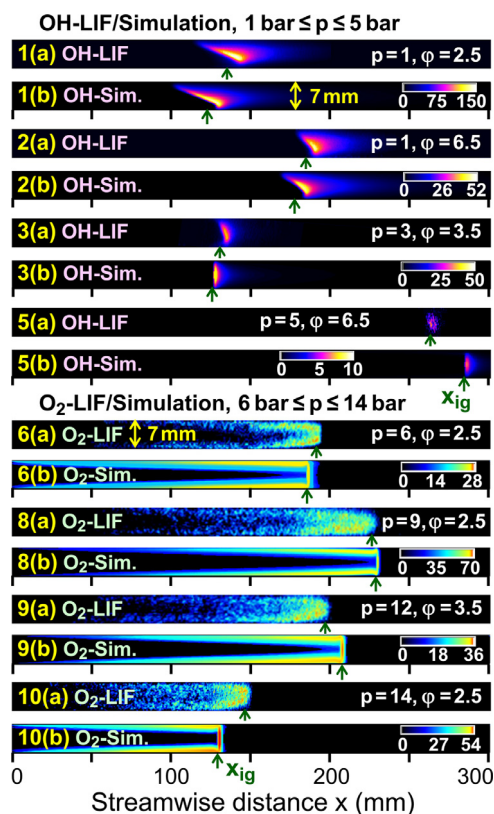
Fig. 9. (1a, 2a, 3a, 5a) OH-LIF and (1b, 2b, 3b, 5b) predicted (ppmv) OH distributions for $1 \leq p \leq 5$ bar, Cases 1, 2, 3 and 5 in Table 1. (6a, 8a, 9a, 10a) hot-O_2-LIF and (6b, 8b, 9b, 10b) predicted (ppmv) hot-O_2 distributions for $6 \leq p \leq 14$ bar, Cases 6, 8, 9 and 10 in Table 1. Vertical arrows marked x_{ig} denote the homogeneous ignition locations. (For interpretation of the references to color in this figure legend, the reader is referred to the web version of this article).

Table 2
Homogeneous ignition distances[a].

Case	p	φ	$x_{ig,exp}$	$x_{ig,sim}$	Δx_{ig} (%)[d]
1[b]	1	2.5	136	124	+8.8
2[b]	1	6.5	185	178	+ 3.8
3[b]	3	3.5	131	126	+3.8
4[b,c]	3	6.5	180	172	+ 4.4
5[b]	5	6.5	264	284	−7.5
6[c]	6	2.5	192	186	+3.1
7[b,c]	6	6.0	254	264	−3.9
8[c]	9	2.5	227	229	−0.9
9[c]	12	3.5	198	208	−5.1
10[c]	14	2.5	147	130	+ 11.6

[a] Measured ($x_{ig,exp}$) and simulated ($x_{ig,sim}$) homogeneous ignition distances (mm) for Cases 1-10 (p in bar)
[b] Cases with –OH-LIF
[c] Cases with O_2-LIF
[d] Percent difference $\Delta x_{ig} = 100 \times (x_{ig,exp} - x_{ig,sim})/x_{ig,exp}$

the G rates were constructed by integrating the volumetric hydrogen gaseous reaction rates over the entire 7-mm channel height. Measured temperature profiles of the upper and lower walls are also shown in Fig. 10.

The G conversion profiles extended axially over a length of a few mm only, with the exception of Cases 1 and 2 (axial extents ~20–30 mm, see Fig. 9). This was due to the more pronounced flame asymmetry of these cases, along with the definition of G as the transversely-integrated (over the 7 mm channel height) hydrogen gaseous reaction rate. The rise of the G conversion profiles closely corresponded to the location of homogeneous ignition, as indicated by the arrows marked x_{ig} in Fig. 10 (computed from the 50% rise of OH or hot-O_2), except for Cases 1 and 2 that had stronger flame asymmetries.

The narrow axial extent of the G profiles in Fig. 10 was in stark contrast to hydrogen hetero-/homogeneous combustion at fuel-lean stoichiometries [19, 21], whereby the G conversion rates persisted over the entire post-ignition length $x > x_{ig}$. This was due to the low Lewis number of hydrogen at fuel-lean stoichiometries in air ($Le_{H2} \sim 0.3$): hydrogen was transported more efficiently from the channel core towards the hot walls than heat was transported away from the hot walls, thus confining the gaseous combustion zone close to the catalytic walls and suppressing transverse flame propagation [19]. However, in fuel-rich stoichiometries the deficient oxygen reactant had a Lewis number larger than unity ($Le_{O2} \sim 1.7$–2.2 for the compositions in Table 1) leading to the formation of closed flames extending transversely over the entire channel height. This flame behavior was similar to that observed in fuel-lean hetero-/homogeneous combustion of hydrocarbons in air, where the Lewis number of the deficient fuel was equal to or greater than unity (methane [43], propane [44] and ethane [45]).

The surface coverage profiles for six selected cases in Table 1 are presented in Fig. 11. The surface was mainly covered by Pt(s) and H(s), the latter due to the high sticking coefficient of H_2 on Pt [37] and the continuous presence of the excess H_2 reactant over the entire catalyst length. The large Pt(s) coverage already from $x \approx 0$ manifested that the catalytic reactions were already ignited at the beginning of the catalytic channel. Finally, the minor surface coverages were O(s) and OH(s) in all cases.

4.3. Catalytic processes preceding homogeneous ignition

While assessing the gaseous kinetic model by comparing LIF-measured and predicted homogeneous ignition positions in Fig. 9, it was essential to ensure that the preceding catalytic processes over the gaseous induction zones $0 \leq x < x_{ig}$ were accurately reproduced by the heterogeneous kinetic scheme. This was a principal requirement, since an incorrect prediction of the catalytic reactant depletion over $0 \leq x < x_{ig}$ could greatly impact
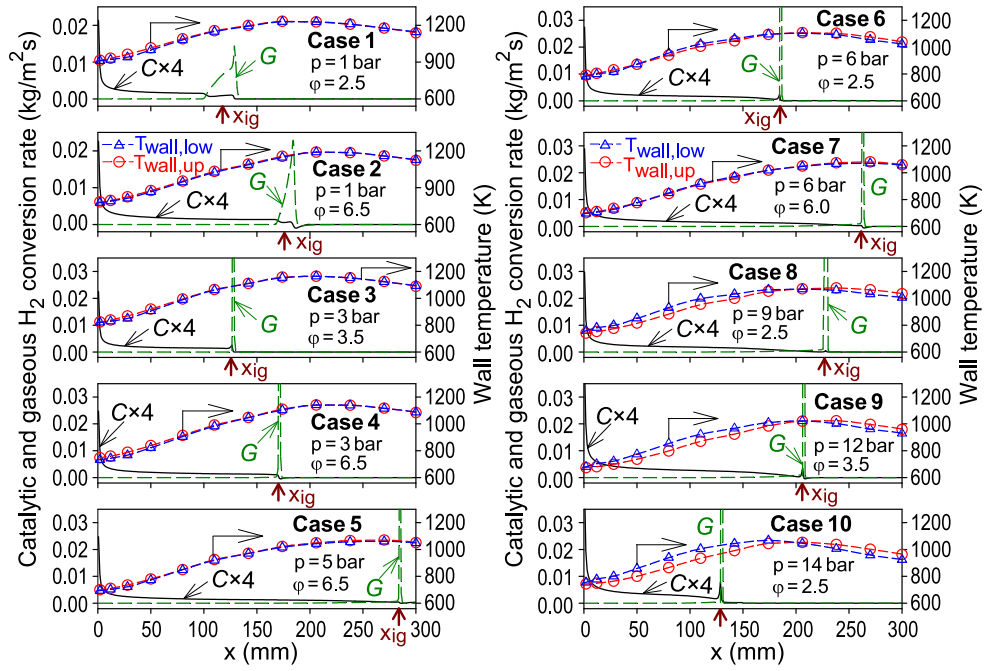
location of homogeneous ignition, which could be unambiguously defined experimentally as discussed previously.

4.2. Comparisons between LIF measurements and numerical predictions

Comparisons between measured and predicted 2-D distributions of the OH radical ($1 \leq p \leq 5$ bar) and of the hot-O_2 ($6 \leq p \leq 14$ bar) are shown in Fig. 9 for those cases in Table 1 where only one LIF technique has been applied. Due to small temperature differences between the upper and lower wall surfaces induced by small differences in the power of the two resistive heaters (typically ± 10 K, as shown by the measured wall temperature profiles in Fig. 10), the flame shapes were modestly asymmetric with the asymmetry being more pronounced at $p = 1$ bar (see Figs. 9(1a) and 9(2a)).

The simulations reproduced the flame asymmetry as shown in Fig. 9(1b) and 9(2b) and they also captured the onset of homogeneous ignition. Computed and measured homogeneous ignition distances are compared in Table 2 for all cases with LIF measurements; the differences between measured and predicted homogeneous ignition distances ranged from 0.9% to 11.6%, thus establishing the aptness of the employed hetero-/homogeneous chemical reaction mechanisms at fuel-rich stoichiometries and pressures up to 14 bar.

The hetero-/homogeneous combustion processes are further elaborated in Fig. 10, providing streamwise profiles of the computed catalytic (C) and gaseous (G) hydrogen conversion rates for all cases with LIF measurements. The C rates referred to the combined contribution of the two catalytic channel walls, while

Fig. 10. Computed streamwise profiles of catalytic (*C*, solid lines) and gas-phase (*G*, dashed lines) hydrogen conversion rates for Cases 1–10. Thermocouple wall measurements (upper wall: circles; lower wall: triangles) and fitted temperature profiles through the thermocouples. Vertical arrows marked x_{ig} denote the homogeneous ignition locations.
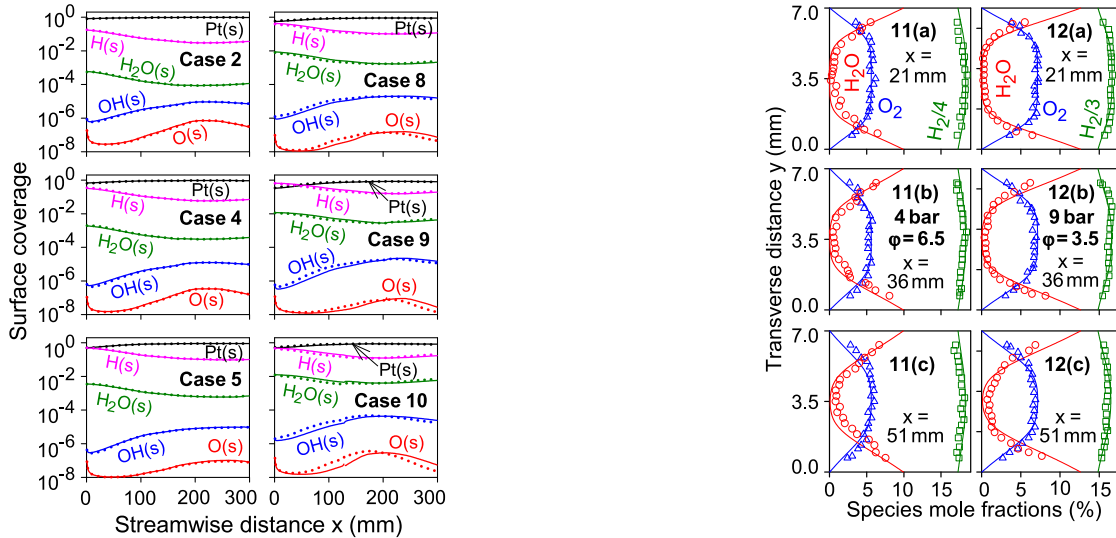

Fig. 11. Computed streamwise profiles of surface coverage for six selected cases in Table 1. Solid lines: upper wall, dotted lines: lower wall.

Fig. 12. Raman-measured (symbols) and simulated (lines) transverse profiles of H_2O, O_2 and H_2 mole fractions for Cases 11 and 12 in Table 1 at three axial positions: (a) $x = 21$ mm, (b) $x = 36$ mm, and (c) $x = 51$ mm. For clarity the hydrogen mole fractions have been divided by 4 and 3 in Cases 11 and 12, respectively.

the location of homogeneous ignition [46]. This key requirement was further compounded by the existence of infinite combinations of catalytic and gaseous reactivities yielding exactly the same homogeneous ignition distance [46]. To this purpose, the comparison between Raman measurements and predictions removed any uncertainty stemming from the catalytic reaction pathway that could potentially falsify the evaluation of gaseous kinetics.

Raman-measured and numerically predicted transverse profiles of H_2, O_2 and H_2O mole fractions are compared in Fig. 12 for Cases 11 and 12 in Table 1 at three axial positions. For clarity, up to 22 Raman data points (out of the total 63 points) are shown for each transverse profile in Fig. 12. The predictions in Fig. 12 indicated a nearly transport-limited catalytic conversion for the deficient reactant O_2, as manifested by the practically vanishing
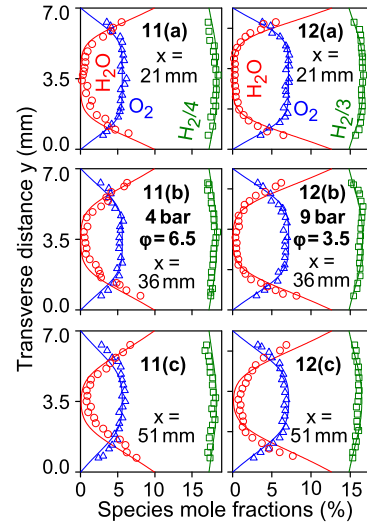
concentrations of O_2 near both catalytic walls ($y = 0$ and 7 mm). This behavior was also attested by the measurements, despite the lack of Raman data closer than 0.7 mm to the catalytic walls. The measured transverse profiles of the reactants H_2 and O_2 and of the product H_2O were well reproduced by the numerical model at all axial positions for the two cases in Fig. 12, demonstrating that the catalytic reaction mechanism was suitable for the investigated rich stoichiometries and elevated pressures.

4.4. Impact of pressure on homogeneous ignition

To understand the impact of pressure on homogeneous ignition, the sole gas-phase ignition characteristics of hydrogen were
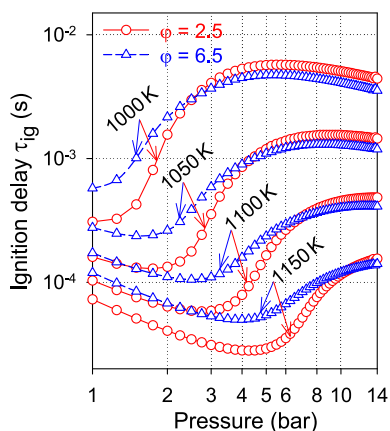
Fig. 13. Ignition delays of fuel-rich H_2/air mixtures computed in a constant pressure batch reactor, as a function of pressure with parameter the initial temperature. Equivalence ratios $\varphi = 2.5$ (circles) and 6.5 (triangles).

firstly investigated, without the inclusion of catalytic reactions. Ignition delays, τ_{ig}, were computed in a constant pressure homogeneous batch reactor using the Senkin package of Chemkin [47]. The ignition delays were defined as the inflection points in the temperature versus time histories. Initial temperatures for the batch reactor simulations were in the range $T_o = 1000$–$1150\,K$, in order to mimic the highest wall temperatures over the gaseous induction zones $0 \leq x < x_{ig}$ in the catalytic channel that preheated the reacting gas; these peak wall temperatures ranged from 995 to $1155\,K$ (see Fig. 10). Computed ignition delays as a function of pressure with parameter the initial temperature are plotted in Fig. 13 for two fuel-rich equivalence ratios ($\varphi = 2.5$ and 6.5).

For the lowest $T_o = 1000\,K$, the ignition delays increased rapidly with rising pressure up to $\sim$3 bar and then changed modestly for $p \geq 3$ bar. For $1050\,K \leq T_o \leq 1150\,K$, the ignition delays initially decreased monotonically with rising pressure, reached a minimum at a critical pressure p_{cr}, and afterwards increased for $p > p_{cr}$. The critical pressure p_{cr} increased with increasing initial temperature (for $\varphi = 2.5$, p_{cr} was 1.75 bar at $T_o = 1050\,K$ and 4.25 bar at $T_o = 1150\,K$, while for $\varphi = 6.5$ it was 1.5 bar at $T_o = 1050\,K$ and 4.0 bar at $T_o = 1150\,K$). This rich non-monotonic behavior of hydrogen gas-phase ignition chemistry as a function of pressure reflected the second and third explosion limits of hydrogen and was an outcome of the competition between the chain branching step $H+O_2 \Leftrightarrow O+OH$, the chain terminating step $H+O_2 +M \Leftrightarrow HO_2 +M$, and also of the chain branching sequence $HO_2 +H_2 \Leftrightarrow H_2O_2 +H$ and $H_2O_2 +M \Leftrightarrow 2OH+M$ that overtook the stability of the HO_2 radical at higher temperatures [27].

The impact of pressure on the homogeneous ignition characteristics in the presence of catalytic reactions was subsequently evaluated. The experimental conditions in Table 1 did not allow for direct assessment of the effect of pressure on homogeneous ignition since the wall temperature profiles could not be held constant (they largely depended on the reactive mixture exothermicity). For this reason, additional hetero-/homogeneous combustion simulations were carried out for selected cases in Table 1, whereby for each case the wall temperatures were kept the same as in Fig. 10 and the inlet conditions were the same as in Table 1 with the exception of the pressure and inlet velocity. The pressure was then artificially altered from its nominal value in Table 1 to values in the full range 1–14 bar, while the inlet velocity was scaled as $U_{IN} \sim 1/p$ in order to maintain, irrespective of pressure, the same mass throughput per unit channel width ($2b\rho_{IN}U_{IN}$), and the same inlet Reynolds number (which will be henceforth based on the channel half-height b). This was necessary to facilitate forthcom-
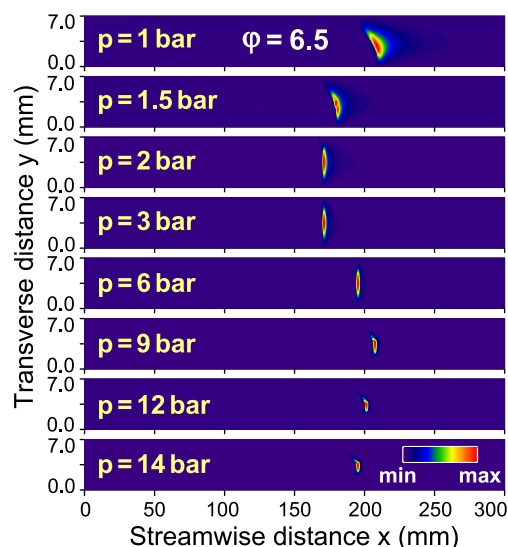

Fig. 14. Predicted OH distributions for the nominal Case 4 in Table 1 ($\varphi = 6.5$, $p_{IN} = 3$ bar, $U_{IN} = 1.48$ m/s) and for the same case at modified pressures and inlet velocities $U_{IN,mod} = U_{IN} \times (p/p_{mod})$. Color bar indicates OH in ppmv, where the minimum is zero and the maximum is: 1 bar: 49.0, 1.5 bar: 46.0, 2 bar: 39.4, 3 bar: 25.3, 6 bar: 11.0, 9 bar: 7.3, 12 bar: 5.2 and 14 bar: 4.2. (For interpretation of the references to color in this figure legend, the reader is referred to the web version of this article).
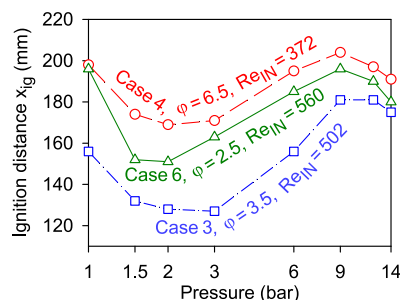

Fig. 15. Predicted ignition distances as a function of pressure for nominal Cases 3, 4 and 6 in Table 1. The nominal pressures p_{IN} and inlet velocities U_{IN} were modified such that $U_{IN,mod} = U_{IN} \times (p/p_{mod})$. In every case, the inlet Reynolds number Re_{IN} (Eq. (3)) was constant.

ing comparisons of the simulations with analytical homogeneous ignition criteria derived for catalytic channels.

Computed distributions of the OH radical for the nominal Case 4 in Table 1 and for the same case at modified pressures and inlet velocities $U_{IN,mod} = U_{IN} \times (p/p_{mod})$ are illustrated in Fig. 14. Since Fig. 14 pertained only to simulations, the OH radical was used to define homogeneous ignition over the entire pressure range. The ignition distances exhibited a non-monotonic dependence on pressure, which is clarified below. Predicted homogeneous ignition distances as a function of pressure are plotted in Fig. 15 for the nominal Case 4 in Fig. 14 and also for the corresponding nominal Cases 3 and 6. In the absence of the catalytic reaction pathway, the shapes in Fig. 15 should have exhibited the same traits as the shapes in Fig. 13 since $x_{ig} \sim \tau_{ig}$. However, there are qualitative differences between Figs. 13 and 15:a) in the high pressure range 9 bar $< p \leq 14$ bar the τ_{ig} either dropped modesty or increased with rising pressure, while x_{ig} always dropped with rising pressure (Fig. 15), and b) while the τ_{ig} at $p = 14$ bar were always longer than those at $p = 1$ bar (see Fig. 13), this was not always the case for x_{ig} (see e.g. Cases 4 and 6 in Fig. 15). The second point was particularly important for large-scale power generation systems as it suggested that homogeneous ignition could be promoted at gas-

turbine relevant pressures ($p \sim 15$ bar) compared to atmospheric pressure applications.

To understand the differences between Figs. 13 and 15, the catalytic pathway had to be accounted for. To this direction, the dependence of the homogeneous ignition distance on the controlling chemical, flow, transport and geometrical parameters will be discussed below. We have developed analytical homogeneous ignition criteria for catalytic channel-flow combustion, initially for transport-limited catalytic conversion of the deficient reactant [48] and subsequently for kinetically-controlled catalytic conversion of the deficient reactant [46]. The ignition criteria were derived using matched activation energy asymptotics, a full 2-D description for the channel geometry, variable transport properties obeying the Chapman-Rubesin conditions [49] $\rho\mu =$ const., $\rho\lambda =$ const., $\rho^2 D_i =$ const., and also constant c_p; this led to a constant Prandtl (Pr) number and constant Lewis numbers (Le_i) for each species. Furthermore, a global gaseous reaction step was considered along with a uniform axial wall temperature profile $T_{WALL}(x) =$ const., and uniform inlet properties.

Since the conversion of the deficient oxygen reactant was practically transport-limited in the present work (as discussed in Fig. 12), the homogeneous ignition criterion from [48] was adopted:

$$G(\zeta_{ig}) = A \frac{1}{Da_g}, \tag{1}$$

with ζ_{ig} a normalized ignition distance, defined as an inverse Graetz number:

$$\zeta_{ig} = \frac{x_{ig}}{b\, Re_{IN}\, Pr}. \tag{2}$$

In Eq. (2) Pr was the constant Prandtl number and Re_{IN} the inlet Reynolds number based on the channel half-height b:

$$Re_{IN} = \rho_{IN} U_{IN} b / \mu_{IN}. \tag{3}$$

In Eq. (1) A was a parameter depending on the constant wall temperature T_{WALL}, the inlet temperature T_{IN} and the heat of reaction. $G(\zeta_{ig})$ was a monotonically increasing function of ζ_{ig} [48] that further included dependencies on the Lewis number (Le) of the deficient reactant, the Prandtl number (Pr) and the ratio (T_{WALL}/T_{IN}). Finally, Da_g was a Damköhler number for gaseous combustion, defined as:

$$Da_g = \tau_{dif} / \tau_{ch}. \tag{4}$$

In Eq. (4) τ_{ch} was a characteristic gas-phase chemical time scale and τ_{dif} a characteristic transverse diffusion time scale:

$$\tau_{dif} = b^2 / \alpha_{th,IN}, \tag{5}$$

with $\alpha_{th,IN}$ the thermal diffusivity of the reactive mixture at the inlet:

$$\alpha_{th,IN} = \lambda_{IN} / \rho_{IN} c_p. \tag{6}$$

The characteristic chemical and diffusion time scales appearing in Eq. (4) clearly demonstrated the competition between gaseous and catalytic reactions for depletion of the deficient reactant: short diffusion times τ_{dif} favored (under transport-limited operation) fast catalytic depletion of the limiting reactant and therefore inhibited gaseous ignition, while short gas-phase chemical times promoted the onset of gaseous ignition. Since $\alpha_{th,IN}$ in Eq. (6) was inversely proportional to pressure, Eqs. (1), (4) and (5) yielded $G(\zeta_{ig}) \sim \tau_{ch}/p$ and because $G(\zeta_{ig})$ was a monotonically increasing function of ζ_{ig} that could be linearized with good accuracy over the range of ignition distances in Fig. 15, the following relationship could be deduced:

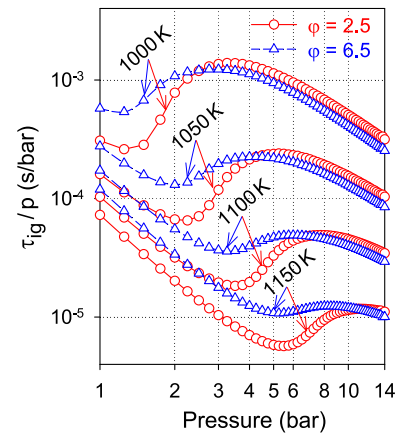$$\zeta_{ig} \sim \tau_{ch}/p. \tag{7}$$

Fig. 16. Ignition delays divided by pressure for fuel-rich H_2/air mixtures computed in a constant pressure batch reactor, as a function of pressure with parameter the initial temperature. Equivalence ratios $\varphi = 2.5$ (circles) and 6.5 (triangles).

Each individual plot in Fig. 15 had, by construction, the same Re_{IN} such that according to Eq. (2) $\zeta_{ig} \sim x_{ig}$ and thus:

$$x_{ig} \sim \tau_{ch}/p. \tag{8}$$

Therefore, the presence of the catalytic pathway introduced a scaling factor $1/p$ between the gaseous chemical time τ_{ch} and the homogeneous ignition distance x_{ig}. Considering that $\tau_{ch} \sim \tau_{ig}$, a scaled plot τ_{ig}/p is constructed in Fig. 16. It is evident that this plot compared more favorably with Fig. 15 and, in particular, it reproduced the appreciable drop in x_{ig} ($\sim \tau_{ch}/p$) above 9 bar. Of course the agreement was qualitative since in the simulations of Fig. 15 the wall temperatures were not uniform along the channel (see Fig. 10), while the ignition criterion in Eq. (1) considered a uniform wall temperature T_{WALL}.

For gas turbines in large-scale power generation (~ 15 bar), homogeneous ignition was more favorable compared to atmospheric pressure systems as seen in Fig. 16. Moreover, for small-turbines of mesoscale power generation systems (pressures 2–5 bar), the results in Fig. 16 suggested an even stronger promotion of homogeneous ignition at least for the lower equivalence ratio $\varphi = 2.5$ and initial temperatures $T_o \geq 1050$ K. These factors had to be considered when designing catalytic-rich/gaseous lean burners for power generation systems.

Finally, sensitivity analysis (SA) was performed in a surface perfectly stirred reactor (SPSR) [50] in order to identify the key surface and gas-phase reactions affecting homogeneous combustion. The selected SPSR conditions mimicked the channel experiments. To this direction, the surface temperature of the SPSR was kept constant at 1100 K (mimicking typical highest catalyst temperatures over the gaseous induction zones in the channel, see Fig. 10), while the inlet SPSR temperature was also set to 1100 K. By fixing the surface temperature the exothermicity of the catalytic pathway was suppressed, thus allowing the investigation of the SPSR temperature changes due to gaseous combustion alone. The bulk gas SPSR temperature was computed by solving the energy equation, in which only the gaseous reactions contributed to the heat release. Nonetheless, since both the heterogeneous and the homogeneous reaction pathways produced or destroyed gas-phase species, the computed bulk gas-phase temperature was affected by both reaction pathways. SPSR residence times were selected to achieve approximately equal catalytic and gas-phase conversions for the deficient O_2 reactant, while the SPSR surface-to-volume (S/V) ratio was 0.5 cm^{-1}.

Normalized sensitivity coefficients for the SPSR gas-phase temperature are shown in Fig. 17 for two fuel-rich H_2/air stoichiometries ($\varphi = 2.5$ and 6.5) and two pressures (1 and 14 bar).
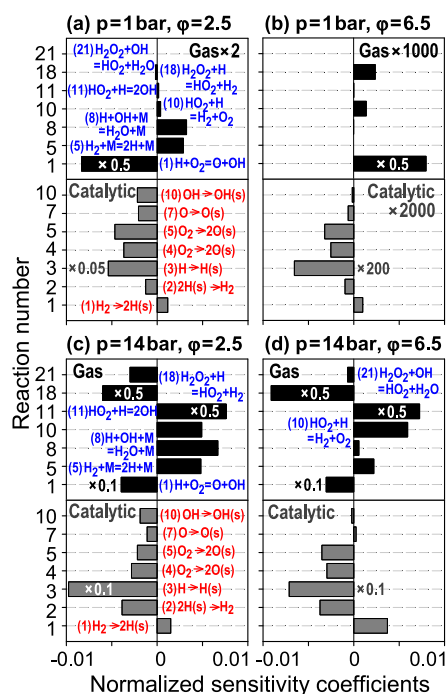
Fig. 17. Normalized sensitivity coefficients for the gas-phase temperature in a surface perfectly stirred reactor (SPSR) at two pressures (1 and 14 bar) and two equivalence ratios (2.5 and 6.5). Coefficients for the main gas-phase and main surface reactions are shown.

In terms of catalytic chemistry, the adsorption/desorption of H_2 (reactions 1 and 2), the adsorption of O_2 (duplicate reactions 4 and 5), and the adsorption of H radical (reaction 3) were the most sensitive. Hydrogen adsorption (reaction 1) had a positive sensitivity coefficient since an increase of its rate led to enhanced surface blockage by H(s) thus inhibiting adsorption of the limiting O_2 reactant; this in turn led to reduced catalytic conversion of O_2 and hence to increased gaseous consumption of O_2 and to increased gaseous heat release. Conversely, the adsorption of O_2 (reactions 4 and 5) had a negative sensitivity coefficient. The adsorption of H (reaction 3) had a strong negative sensitivity coefficient as it deprived this important radical from the gaseous radical pool. In terms of gaseous chemistry, the most sensitive reactions were those involving production or depletion of the H radical.

5. Conclusions

The catalytic and gaseous combustion of $H_2/O_2/N_2$ mixtures was investigated experimentally and numerically in a Pt-coated channel at fuel-rich stoichiometries (equivalence ratios $\varphi = 2.5$-6.5) and pressures 1–14 bar. 1-D Raman measurements of major gas-phase species concentrations assessed the heterogeneous combustion processes, while planar LIF of either OH or of hot-O_2 monitored the onset of homogeneous ignition. Simulations were carried out using a 2-D code with detailed heterogeneous and homogeneous chemistry and transport. The following are the key conclusions.

(1) The combination of OH-LIF at pressures below $\sim$5 bar and of hot O_2-LIF at pressures higher than $\sim$5 bar could accurately determine the homogeneous ignition locations over the entire pressure range (1–14 bar). This was because the OH-LIF signal was quenching-dominated at elevated pressures, while the hot O_2-LIF signal was predissociation-controlled thus allowing adequate signal-to-noise ratios even at the highest investigated pressures.

(2) Both Raman measurements and numerical simulations demonstrated a transport-limited catalytic conversion of the defi-

cient O_2 reactant over the gas-phase ignition induction zones, in which the wall temperatures ranged between $\sim$800 K and $\sim$1100 K. The transport-limited catalytic depletion of O_2 led to increased fuel-rich equivalence ratios (up to $\varphi = 19.8$) at the locations of homogeneous ignition.

(3) Good agreement has been established between measured and predicted homogeneous ignition distances (within 12%) and flame shapes, thus attesting the aptness of the employed hetero-/homogeneous chemical reaction mechanisms at fuel-rich stoichiometries and elevated pressures.

(4) Gaseous combustion propagated to the channel center and extended axially over a length of only a few mm due to the predominantly vertical direction of the formed flames. This was in contrast to earlier fuel-lean $H_2/O_2/N_2$ hetero-/homogeneous combustion studies, wherein the ensuing flames were confined close and parallel to the horizontal catalytic walls and extended axially over substantial fractions of the channel length. This difference was an outcome of the Lewis number of the deficient reactant, which was less than unity for the fuel-lean stoichiometries and greater than unity for the fuel-rich ones.

(5) Analytical homogeneous ignition criteria have shown that the catalytic reaction pathway introduced a scaling factor $1/p$ to the homogeneous ignition distances x_{ig}. This behavior, in conjunction with the intricate pressure dependence of the gaseous ignition chemistry of hydrogen, led to generally shorter homogeneous ignition distances at 14 bar compared to 1 bar. This had practical implications for gas-turbine burners utilizing the catalytic-rich/gaseous-lean combustion concept for large-scale power generation ($\sim$15 bar), as it suggested that gas-phase combustion could be initiated within the catalytic module. For mesoscale power generation with operating pressures of 2–5 bar, homogeneous ignition could become even more favorable compared to either 1 or 14 bar, at least for certain fuel-rich stoichiometries.

(6) Sensitivity analysis carried out in a surface perfectly stirred reactor (SPSR) identified the key surface and gaseous reactions affecting the gas temperature. Hydrogen and oxygen adsorption/desorption and adsorption of the H radical were the most sensitive catalytic reactions, while most sensitive gaseous reactions were those involving the H radical.

References

[1] W.C. Pfefferle, L.D. Pfefferle, Catalytically stabilized combustion, Prog. Energy Combust. Sci. 12 (1986) 25–41.
[2] K.W. Beebe, K.D. Cairns, V.K. Pareek, S.G. Nickolas, J.C. Schlatter, T. Tsuchiya, Development of catalytic combustion technology for single-digit emissions from industrial gas turbines, Catal. Today 59 (2000) 95–115.
[3] S. Eriksson, M. Wolf, A. Schneider, J. Mantzaras, F. Raimondi, M. Boutonnet, S Järas, Fuel rich catalytic combustion of methane in zero emissions power generation processes, Catal. Today 117 (2006) 447–453.
[4] L.L. Smith, H. Karim, M.J. Castaldi, S. Etemad, W.C. Pfefferle, Rich-catalytic lean-burn combustion for fuel-flexible operation with ultra-low emissions, Catal. Today 117 (2006) 438–446.
[5] A. Schneider, J. Mantzaras, R. Bombach, S. Schenker, N. Tylli, P. Jansohn, Laser induced fluorescence and Raman measurements of major species during partial catalytic oxidation of methane with large H_2O and CO_2 dilution at pressures up to 10 bar, Proc. Combust. Inst 31 (2007) 1973–1981.
[6] F. Bolaños, D. Winkler, F. Piringer, T. Griffin, R. Bombach, J. Mantzaras, Study of a rich/lean staged combustion concept for hydrogen at gas turbine relevant conditions, ASME GT2013-94420, San Antonio Texas, USA, June 3–7, 2013.
[7] A. Schneider, J. Mantzaras, S. Eriksson, Ignition and extinction in catalytic partial oxidation of methane-oxygen mixtures with large H_2O and CO_2 dilution, Combust. Sci. Technol. 180 (2008) 89–126.
[8] T. Griffin, D. Winkler, M. Wolf, C. Appel, J. Mantzaras, Staged catalytic combustion method for the advanced zero emissions gas turbine power plant, ASME GT2004-54101, Vienna, Austria, June 14–17, 2004.

[9] S.K. Alavandi, S. Etemad, B.D. Baird, Low single digit NOx emissions catalytic combustor for advanced hydrogen turbines for clean coal power systems, ASME GT2012-68128, Copenhagen, Denmark, June 11–15, 2012.

[10] K. Maruta, Micro and mesoscale combustion, Proc. Combust. Inst 33 (2010) 125–150.

[11] G. Pizza, C.E. Frouzakis, J. Mantzaras, A.G. Tomboulides, K. Boulouchos, Three-dimensional simulations of premixed hydrogen/air flames in microtubes, J. Fluid Mech. 658 (2010) 463–491.

[12] Y.G. Ju, K. Maruta, Microscale combustion: Technology development and fundamental research, Prog. Energy Combust. Sci. 37 (2011) 669–715.

[13] A. Brambilla, M. Schultze, C.E. Frouzakis, J. Mantzaras, R. Bombach, K. Boulouchos, An experimental and numerical investigation of premixed syngas combustion dynamics in mesoscale channels with controlled wall temperature profiles, Proc. Combust. Inst 35 (2015) 3429–3437.

[14] G. Pizza, J. Mantzaras, C.E. Frouzakis, A.G. Tomboulides, K. Boulouchos, Suppression of combustion instabilities of premixed hydrogen/air flames in microchannels using heterogeneous reactions, Proc. Combust. Inst 32 (2009) 3051–3058.

[15] G. Pizza, J. Mantzaras, C.E. Frouzakis, Flame dynamics in catalytic and non-catalytic mesoscale microreactors, Catal. Today 155 (2010) 123–130.

[16] P.A. Bui, D.G. Vlachos, P.R. Westmoreland, Homogeneous ignition of hydrogen/air mixtures over platinum, Proc. Combust. Inst 26 (1996) 1763–1770.

[17] N. Meynet, A. Bentaib, V. Giovangigli, Impact of oxygen starvation on operation and potential gas-phase ignition of passive auto-catalytic recombiners, Combust. Flame 161 (2014) 2192–2202.

[18] J.C.G. Andrae, P.H Björnbom, Wall effects of laminar hydrogen flames over platinum and inert surfaces, AIChE J 46 (2000) 1454–1460.

[19] C. Appel, J. Mantzaras, R. Schaeren, R. Bombach, A. Inauen, B. Kaeppeli, B. Hemmerling, A. Stampanoni, An experimental and numerical investigation of homogeneous ignition in catalytically stabilized combustion of hydrogen/air mixtures over platinum, Combust. Flame 128 (2002) 340–368.

[20] J. Mantzaras, R. Bombach, R. Schaeren, Hetero-/homogeneous combustion of hydrogen/air mixtures over platinum at pressures up to 10 bar, Proc. Combust. Inst 32 (2009) 1937–1945.

[21] Y. Ghermay, J. Mantzaras, R. Bombach, K. Boulouchos, Homogeneous combustion of fuel lean $H_2/O_2/N_2$ mixtures over platinum at elevated pressures and preheats, Combust. Flame 158 (2011) 1491–1506.

[22] Y. Ghermay, J. Mantzaras, R. Bombach, Effects of hydrogen preconversion on the homogeneous ignition of fuel-lean $H_2/O_2/N_2/CO_2$ mixtures over platinum at moderate pressures, Combust. Flame 157 (2010) 1942–1958.

[23] M. Maestri, A. Beretta, T. Faravelli, G. Groppi, E. Tronconi, Role of gas-phase chemistry in the rich combustion of H_2 and CO over a Rh/Al_2O_3 catalyst in annular reactor, Chem. Eng. Sci. 62 (2007) 4992–4997.

[24] M. Maestri, A. Beretta, T. Faravelli, G. Groppi, E. Tronconi, D.G. Vlachos, Two-dimensional detailed modeling of fuel-rich H_2 combustion over Rh/Al_2O_3 catalyst, Chem. Eng. Sci. 63 (2008) 2657–2669.

[25] M. Schultze, J. Mantzaras, R. Bombach, K. Boulouchos, An experimental and numerical investigation of the hetero-/homogeneous combustion of fuel-rich hydrogen/air mixtures over platinum, Proc. Combust. Inst 34 (2013) 2269–2277.

[26] M. Schultze, J. Mantzaras, F. Grygier, R. Bombach, Hetero-/homogeneous combustion of syngas mixtures over platinum at fuel-rich stoichiometries and pressures up to 14 bar, Proc. Combust. Inst 35 (2015) 2223–2231.

[27] I. Glassman, R.A. Yetter, N.G. Glumac, Combustion, Fifth Ed., Academic Press, London, 2014.

[28] M. Reinke, J. Mantzaras, R. Schaeren, R. Bombach, A. Inauen, S. Schenker, High-pressure catalytic combustion of methane over platinum: in situ experiments and detailed numerical predictions, Combust. Flame 136 (2004) 217–240.

[29] C. Appel, J. Mantzaras, R. Schaeren, R. Bombach, A. Inauen, Turbulent catalytically stabilized combustion of hydrogen/air mixtures in entry channel flows, Combust. Flame 140 (2005) 70–92.

[30] A. Lutz, M. Rupley, R.J. Kee, EQUIL: a Chemkin implementation of STANJAN, for computing chemical equilibria, Sandia National Laboratories, 1996.

[31] J.E.M. Goldsmith, R.J.M. Anderson, Laser-induced fluorescence spectroscopy and imaging of molecular oxygen in flames, Opt. Lett. 11 (1986) 67–69.

[32] M. Di Rosa, K. Klavuhn, R. Hanson, LIF spectroscopy of NO and O_2 in high-pressure flames, Combust. Sci. Technol. 118 (1996) 257–283.

[33] W.P. Partridge, M.S. Klassen, D.D. Thomsen, N.M. Laurendeau, Experimental assessment of O_2 interferences on laser-induced fluorescence measurements of NO in high-pressure, lean premixed flames by use of narrow-band and broad-band detection, Appl. Opt. 35 (1996) 4890–4904.

[34] W.G. Bessler, C. Schulz, V. Sick, J.W. Daily, A versatile modeling tool for nitric oxide LIF spectra, Proceedings of the 3rd Joint Meeting of the U.S. Sections of The Combustion Institute (2003) paper PI05.

[35] J. Mantzaras, C. Appel, P. Benz, Catalytic combustion of methane/air mixtures over platinum: homogeneous ignition distances in channel flow configurations, Proc. Combust. Inst. 28 (2000) 1349–1357.

[36] F.M. Rupley, R.J. Kee, J.A. Miller, Premix: a Fortran program for modeling steady laminar one-dimensional premixed flames, Sandia National Laboratories, 1995 Report No. SAND85-8240.

[37] O. Deutschmann, L.I. Maier, U. Riedel, A.H. Stroemman, R.W. Dibble, Hydrogen assisted catalytic combustion of methane on platinum, Catal. Today 59 (2000) 141–150.

[38] J. Li, Z. Zhao, A. Kazakov, F.L. Dryer, An updated comprehensive kinetic model of hydrogen combustion, Int. J. Chem. Kinet. 36 (2004) 566–575.

[39] M.E. Coltrin, R.J. Kee, F.M. Rupley, Surface Chemkin: a Fortran package for analyzing heterogeneous chemical kinetics at the solid surface-gas phase interface, Sandia National Laboratories, 1996 Report No. SAND90-8003C.

[40] R.J. Kee, F.M. Rupley, J.A. Miller, Chemkin II: a Fortran chemical kinetics package for the analysis of gas-phase chemical kinetics, Sandia National Laboratories, 1996 Report No. SAND89-8009B.

[41] R.J. Kee, G Dixon-Lewis, J Warnatz, M.E. Coltrin, J.A. Miller, A Fortran computer code package for the evaluation of gas-phase multicomponent transport properties, Sandia National Laboratories, 1996 Report No. SAND86-8246.

[42] P.H. Krupenie, The spectrum of molecular oxygen, J. Phys. Chem. Ref. Data 1 (1972) 423–534.

[43] M. Reinke, J. Mantzaras, R. Schaeren, R. Bombach, W. Kreutner, A. Inauen, Homogeneous ignition in high-pressure combustion of methane/air over platinum: comparison of measurements and detailed numerical predictions, Proc. Combust. Inst. 29 (2002) 1021–1029.

[44] S. Karagiannidis, J. Mantzaras, R. Bombach, S. Schenker, K. Boulouchos, Experimental and numerical investigation of the hetero-/homogeneous combustion of lean propane/air mixtures over platinum, Proc. Combust. Inst 32 (2009) 1947–1955.

[45] X. Zheng, J. Mantzaras, R. Bombach, Hetero-/homogeneous combustion of ethane/air mixtures over platinum at pressures up to 14 bar, Proc. Combust. Inst 34 (2013) 2279–2287.

[46] J. Mantzaras, C. Appel, Effects of finite rate heterogeneous kinetics on homogeneous ignition in catalytically stabilized channel-flow combustion, Combust. Flame 130 (2002) 336–351.

[47] A.E. Lutz, R.J. Kee, J.A. Miller, Senkin: a Fortran program for predicting homogeneous gas phase chemical kinetics with sensitivity analysis, Sandia National Laboratories, 1996 Report No. SAND87-8248.

[48] J. Mantzaras, P. Benz, An asymptotic and numerical investigation of homogeneous ignition in catalytically stabilized channel flow combustion, Combust. Flame 119 (1999) 455–472.

[49] D.R. Chapman, M.W. Rubesin, Temperature and velocity profiles in the compressible laminar boundary layer with arbitrary distribution of surface temperature, J. Aeronaut. Sci. 16 (1949) 547–565.

[50] H.K. Moffat, R.J. Kee, J.F. Grcar, J.A. Miller, Surface PSR: a Fortran program for modeling well-stirred reactors with gas and surface reactions, Sandia National Laboratories, 1993 Report No. SAND91-8001.